The 9th European Congress on Computational Methods in Applied Sciences and Engineering
ECCOMAS Congress 2024
3–7 June 2024, Lisboa, Portugal

SPECTRAL ANALYSIS FOR HIGH-ORDER FLUX RECONSTRUCTION METHODS

Romaric SIMO TAMOU[1,2], Vincent PERRIER[2], Quang Huy TRAN[1], Julien BOHBOT[1] and Julien COATLEVEN[1]

[1] IFP Énergies Nouvelles (IFPEN)
1 et 4 avenue de Bois-Préau, 92852 Rueil-Malmaison, France
e-mail: romaric.simo-tamou@ifpen.fr, quang-huy.tran@ifpen.fr, julien.bohbot@ifpen.fr, julien.coatleven@ifpen.fr

[2] Institut national de recherche en sciences et technologies du numérique (INRIA)
Université de Pau et des Pays de l'Adour
LMAP UMR 5142 – Avenue de l'Université, 64013 Pau, France
email: vincent.perrier@inria.fr, romaric.simo-tamou@inria.fr

Key words: Flux Reconstruction methods, Spectral analysis, Turbulent flows, Direct Numerical Simulation, Multi-species mixture

1 INTRODUCTION

In the industrial sector, computational fluid dynamics (CFD) experts are increasingly focused on conducting high-fidelity simulations to address turbulent flow challenges. Most industrial codes employ lower-order methods, typically with an accuracy order of less than two. This approach is justified by the extensive work carried out between the 1970s and 1990s, which made these low-order schemes both robust and efficient [1]. there is a broad spectrum of physical problems where low-order methods are not adequate. For instance, in vortex-dominated flows, the limitation in accuracy becomes a significant obstacle, necessitating fine meshing to accurately capture small-scale turbulent eddies. Additionally, low-order numerical schemes tend to introduce numerical dissipation errors, which can compromise the integrity of the simulation results, potentially rendering them unusable.

To overcome this major obstacle, many high-order numerical schemes with compact stencil have been developed, including Discontinuous Galerkin (DG) schemes [2, 3, 4], Spectral Difference (SD) schemes [5, 6, 7], and Flux Reconstruction (FR) schemes [8, 9, 10]. By construction, these schemes are highly accurate and can significantly reduce numerical dissipation and dispersion, thus allowing the use of coarser and less expensive meshes. Finally, DG, SD, and FR schemes parallelize efficiently and allow for the full utilization of the computing power provided by current parallel architectures

The spectral properties allow for the analysis of how accurately a scheme represents wave propagation by evaluating its effects on numerical dispersion and dissipation. In particular, they are essential for determining the stability, the fidelity of numerical solutions,

and the scheme's ability to accurately resolve the fine details of a wave or disturbance. With the exception of spectral methods, most numerical methods preserve the dispersion relation only for low wavenumbers, and introduce significant dispersion and/or dissipation beyond a critical wavenumber denoted as the resolving efficiency.

Huynh [9] was the first to explore the spectral properties of FR schemes, using Fourier analysis on 1-D advection with fully upwinded Riemann flux at the interface to identify both principal and spurious eigenvalues. A direct modal analysis of the FR formulation was conducted by Asthana et al [8] to determine dispersion, dissipation and energy fractions corresponding to the numerical modes.

In this paper, we perform new analyses of their dissipation and dispersion properties based on space–time spectral analysis for high-order FR schemes, and we find consistent results with the classical analysis. Finally, we extend and validate these results for academic configurations of multi-species flows and turbulent flows.

2 Flux Reconstruction

2.1 General Formulation

We consider the first-order conservation law

$$\frac{\partial u}{\partial t} + \frac{\partial f(u)}{\partial x} = 0, \tag{1}$$

with the physical coordinates $x \in \Omega \subset \mathbb{R}$ and time t. The nonlinear flux f depends on the quantity of interest u. Following the original work by Huynh [9], we describe here the one-dimensional flux reconstruction formulation. We consider a partition of Ω into N elements Ω_n such that

$$\overline{\Omega} = \bigcup_{n=0}^{N-1} \overline{\Omega}_n, \tag{2}$$

with

$$\Omega_n = \{x \in \mathbb{R} \mid x_n < x < x_{n+1}\}. \tag{3}$$

Restricting in Ω_n, we approach the solution by a polynomial of degree p denoted $u_n^{\delta D}$ in Ω_n and zero elsewhere. This polynomial should approximate the system (1) in Ω_n. All calculations are performed in the reference element $\widehat{\Omega}$

$$\widehat{\Omega} = \{\hat{x} \in \mathbb{R} \mid -1 < \hat{x} < 1\}. \tag{4}$$

using the isoparametric transformation Θ_n allowing the passage of an element $\widehat{\Omega}$ to Ω_n. The isoparametric transformation Θ_n that maps the reference element $\widehat{\Omega}$ to the physical element Ω_n is given by

$$x = \Theta_n(\hat{x}) = \frac{(x_{n+1} - x_n)\hat{x}}{2} + \frac{(x_{n+1} + x_n)}{2}.$$

The Jacobian of this transformation is denoted by $J_n = \frac{d\Theta_n}{d\hat{x}} = \frac{1}{2}(x_{n+1} - x_n)$. By definition of Ω_n, J_n is non-zero, and Θ_n is invertible. An illustration of the transformation from $\widehat{\Omega}$ to Ω_n is provided in Figure 1. Using this transformation, we write the conservation law (1) on the reference element $\widehat{\Omega}$

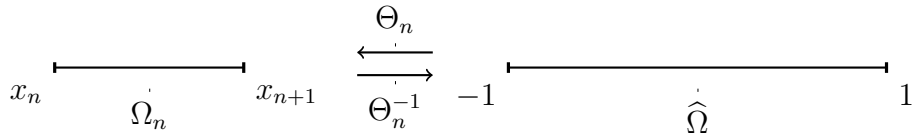

Figure 1: Transformation from an element Ω_n to the reference element $\widehat{\Omega}$ in 1D.

$$\frac{\partial \hat{u}_n^{\delta D}}{\partial t} + \frac{\partial \hat{f}_n^{\delta D}}{\partial \hat{x}} = 0, \tag{5}$$

with new variables

$$\hat{u}_n^{\delta D}(t, \hat{x}) = J_n u_n^{\delta D}(t, \Theta_n(\hat{x})), \tag{6a}$$
$$\hat{f}_n^{\delta D}(t, \hat{x}) = f_n^{\delta D}(t, \Theta_n(\hat{x})). \tag{6b}$$

In order to lighten the writing, we will now remove the notation index n referring to the element Ω_n when there is no ambiguity. which allows us to rewrite (5) as

$$\frac{\partial \hat{u}^{\delta D}}{\partial t} + \frac{\partial \hat{f}^{\delta D}}{\partial \hat{x}} = 0. \tag{7a}$$

Flux Reconstruction methods use a nodal basis of degree p to approch the solution within each element of a given grid. Consider the $N_p = p + 1$ distinct interior points $\hat{x}_i$, $0 \leq i \leq p$, again called solution points of $\widehat{\Omega}$. We assume that the transform of the discontinuous solution is known at time t at these N_p points, and we note it $\hat{u}_i^{\delta D} = \hat{u}^{\delta D}(t, \hat{x}_i)$. Therefore, we can approach the solution by interpolating it at the N_p solution points

$$\hat{u}^{\delta D} = \sum_{i=0}^{p} \hat{u}_i^{\delta D} l_i(\hat{x}), \tag{8}$$

where the Lagrange polynomials $l_i(\hat{x})$ of degree p is defined by

$$l_i(\hat{x}) = \prod_{k=0, k\neq i}^{p} \frac{\hat{x} - \hat{x}_k}{\hat{x}_i - \hat{x}_k}. \tag{9}$$

The solution points are chosen to be the 1D Gauss–Legendre, Figure 2 shows the solution and flux point locations in the reference element for $p = 2$.

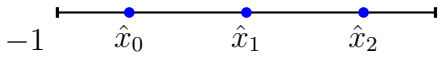

Figure 2: Reference element $\widehat{\Omega}$, for $p = 2$.

The approximation of degree p by cell of the flux using the values of the solution at the N_p inner points is

$$\hat{f}^{\delta D} = \sum_{k=0}^{p} \hat{f}_k^{\delta D} l_k, \tag{10}$$

where $\hat{f}_k^{\delta D} = \hat{f}(t, \hat{x}_k)$. The principle of the FR scheme as presented in [9] consists in writing problem (7) at N_p solution points by:

$$\left(\frac{\partial \hat{u}^{\delta D}}{\partial t} + \frac{\partial \hat{f}^{\delta}}{\partial \hat{x}} \right) (\hat{x}_k) = 0, \tag{11}$$

where the divergence of the flux is written as

$$\frac{\partial \hat{f}^{\delta}}{\partial \hat{x}} = \sum_{k=0}^{p} \hat{f}_k^{\delta D} \frac{dl_k}{d\hat{x}} + (\hat{f}_L^{\delta I} - \hat{f}_L^{\delta D}) \frac{dh_L}{d\hat{x}} + (\hat{f}_R^{\delta I} - \hat{f}_R^{\delta D}) \frac{dh_R}{d\hat{x}}, \tag{12}$$

with $\hat{f}_L^{\delta D} = \hat{f}^{\delta D}(t, -1)$ and $\hat{f}_R^{\delta D} = \hat{f}^{\delta D}(t, 1)$ are the extrapolated values of the discontinuous flux transform, and $\hat{f}_L^{\delta I}$ and $\hat{f}_R^{\delta I}$ are the values of the common numerical flux transform at the interfaces. The common flux at each interface is computed using a Riemann solver that takes as input the solution values from the cells adjacent to the interface under consideration. For example, one can use the Roe solver [11] or the Lax-Friedrichs approach [12, 13] for the Euler or advection equations.

The VCJH [10] correction functions are given by

$$h_L = \frac{(-1)^p}{2} \left[L_p - \left(\frac{\eta_p L_{p-1} + L_{p+1}}{1 + \eta_p} \right) \right], h_R = \frac{1}{2} \left[L_p + \left(\frac{\eta_p L_{p-1} + L_{p+1}}{1 + \eta_p} \right) \right], \tag{13}$$

where L_p is the normalized Legendre polynomial of degree p, $L_p(1) = 1$, and

$$\eta_p = \frac{c(2p+1)(a_p p!)^2}{2}, a_p = \frac{(2p!)}{2^p (p!)^2}, \tag{14}$$

and c is a free parameter satisfying

$$\frac{-2}{(2p+1)(a_p p!)^2} < c < +\infty. \tag{15}$$

The parameter c thus defined allows for a family of FR schemes, and some clever choices allow retrieving known high-order schemes, in the case of problems with linear fluxes as presented in Table 1.

c	0	$\frac{2p}{(2p+1)(p+1)(a_p p!)^2}$	$\frac{2(p+1)}{(2p+1)p(a_p p!)^2}$
High order scheme	Nodal DG	SD	Huynh

Table 1: Higher-order schemes obtained from the correction function parameter c.

The correction functions (13) allow us to impose the values $\hat{f}_L^{\delta I}$ and $\hat{f}_R^{\delta I}$ of the common numerical flux transform at the interfaces. This will shift the flux discontinuity from the interfaces to the interior of the elements. An illustration of the flux reconstruction is given in Figure 3.

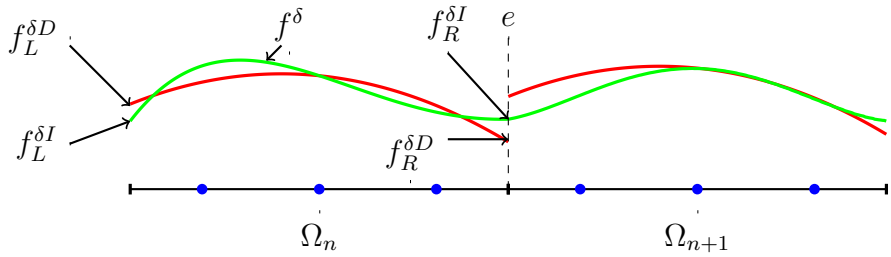

Figure 3: Reconstruction of the continuous flux at the interface e.

3 Spectral analysis

3.1 Methodology

We consider the linear advection equation in a periodic domain with a harmonic initial solution

$$\frac{\partial u}{\partial t} + \frac{\partial u}{\partial x} = 0, \tag{16a}$$

$$u(0,x) = e^{\mathrm{j}kx}, \tag{16b}$$

where k the constant wavenumber and $\mathrm{j}^2 = -1$. Problem (16a) is obtained from problem (1) by using the flux function $f(u) = u$.

We start by spatially discretizing equation (16a) using the FR scheme. For simplicity in notation and without loss of generality, we assume that the interval Ω_n has a length $\Delta x_n = \Delta x$, and the flux at interfaces follows the upwind scheme. Applying the FR schemes methodology from subsection 3.1 to (16a) on the reference element $\hat{\Omega}$, we write it in matrix form:

$$\frac{d\hat{\mathbf{u}}_n^{\delta}}{dt} = -\frac{2}{\Delta x}\mathbf{D}\hat{\mathbf{u}}_n^{\delta} - \frac{2}{\Delta x}\mathbf{h_L}(\mathbf{l}^T\hat{\mathbf{u}}_{n-1}^{\delta} - \mathbf{l}^T\hat{\mathbf{u}}_n^{\delta}), \tag{17}$$

Runge Kutta Schemes	RK33	RK44	RK45
G	$\sum_{i=0}^{3} \frac{(\Delta t\mathbf{M})^i}{i!}$	$\sum_{i=0}^{4} \frac{(\Delta t\mathbf{M})^i}{i!}$	$\sum_{i=0}^{4} \frac{(\Delta t\mathbf{M})^i}{i!} + \frac{(\Delta t\mathbf{M})^5}{200}$

Table 2: The spatio-temporal transfer matrix $\mathbf{G}$.

with

$$\mathbf{D}[i,n] = \frac{dl_n}{d\hat{x}}(\hat{x}_i), \quad \hat{\mathbf{u}}_n^{\delta}[i] = \hat{u}_n^{\delta D}(\hat{x}_i), \quad \mathbf{l}[i] = l_i(-1), \quad \mathbf{h_L}[i] = \frac{dh}{d\hat{x}}(-1), \quad 1 \leq i, n \leq p+1. \tag{18}$$

The exact solution to problem (16) is:

$$u(t,x) = e^{\mathrm{j}k(x-t)}. \tag{19}$$

However, the numerical solution given by (17) is

$$\hat{\mathbf{u}}_n^{\delta}(t) = e^{\mathrm{j}(k\Delta x - \omega^{\delta}(k)t)}\mathbf{v}, \tag{20}$$

where $\omega^{\delta}(k)$ is a complex number that expresses the numerical wave frequency. $\mathbf{v}$ is a vector associated with the projection of the numerical solution onto the basis of nodal functions. By substituting (20) into (17), and setting

$$\mathbf{M} = -\frac{2}{\Delta x}(\mathbf{D} - \mathbf{h_L}\mathbf{l}^T + e^{-\mathrm{j}k^{\delta}\Delta x}\mathbf{h_L}\mathbf{l}^T), \tag{21a}$$

$$\frac{d\hat{\mathbf{u}}_n^{\delta}}{dt} = \mathbf{M}\hat{\mathbf{u}}_n^{\delta}. \tag{21b}$$

Next, we discretize (21b) in time using a Runge-Kutta method, and we write

$$\hat{\mathbf{u}}_n^{\delta}(t_{s+1}) = \mathbf{G}\hat{\mathbf{u}}_n^{\delta}(t_s), \tag{22}$$

with $t_{s+1} = t_s + \Delta t$. The spatio-temporal transfer matrix $\mathbf{G}$ is defined by the matrix $\mathbf{M}$ and the Runge-Kutta method used in Table 2.

3.2 Matrix power method for the spectral analysis

The Matrix Power Multiplication (MPM) is a technique used to compute the successive powers of a matrix. It leverages these matrix multiplications to achieve various goals, such as determining the convergence of matrix powers or identifying the dominant eigenvalues, often through successive iterations. The MPM was used by Vanharena et al. [14] for the spectral analysis of high-order spectral discontinuous methods.

According to subsection 3.1, the solution at time t_{s+1} is calculated using the solution at time t_s and the spatio-temporal discretization matrix $\mathbf{G}$ using the relation (22). By applying this process recursively, it follows that the solution at time t_{s+1} can be obtained by applying the sth power of the matrix $\mathbf{G}$ to the initial solution.

$$\hat{\mathbf{u}}_n^{\delta}(t_{s+1}) = \mathbf{G}^s\hat{\mathbf{u}}_n^{\delta}(t=0). \tag{23}$$

Hypothesis: We assume that the matrix $\mathbf{G}$ satisfies the eigenvalue problem $\mathbf{G}v_l = \lambda_l v_l$, where for $l \in \{0, 1, \cdots, p\}$, $\lambda_l \in \mathbb{C}$ and $v_l \in \mathbb{C}^{(p+1)}$. We also assume that the $p+1$ eigenvectors v_l span $\mathbb{C}^{(p+1)}$ and that the eigenvalues satisfy: $|\lambda_0| < |\lambda_l|$ and $|\lambda_l| < |\lambda_p|$ for $l \notin \{0, p\}$. Then, for any initial condition

$$\hat{u}_n^\delta(t=0) = \sum_{l=0}^{p} \alpha_l^0 v_l, \text{ with } \alpha_p^0 \neq 0, \tag{24}$$

we have the approximation [14] of (23) as $s \to +\infty$

$$\hat{u}_n^\delta \approx \alpha_p^0 \lambda_p^s v_p. \tag{25}$$

This result indicates that as the number of temporal iterations becomes large, $\hat{u}_n^\delta$ behaves similarly to $\alpha_p^0 \lambda_p^s v_p$.

Conclusion: Under the previous hypothesis, spectral analysis of FR schemes can be performed using the properties of the eigenvalue λ_p. The criteria for measuring dispersion and dissipation relations are

$$1 - \rho = 0, \tag{26}$$

$$|k\Delta x - \phi| = 0, \tag{27}$$

where $\rho = \lambda_p$ and $\phi = -\arg(\lambda_p)/\mathsf{CFL}$.

3.3 Effect of Polynomial Order

The dissipation and dispersion relations for each SD scheme via FR are drawn in Figure 4 by varying the polynomial degrees $p \in \{2, 5\}$. It is observed that for all polynomial degrees, the dispersion and dissipation relation are well approximated for low wavenumbers. However, as the order increases, the scheme has difficulty accurately approximating the exact relation for a range of high wavenumbers. These findings are consistent with those reported by Jameson [8].

3.4 Effect of Correction Function

The dissipation and dispersion relations are plotted in Figure 5. It is observed that the exact mode is relatively well approximated for low wavenumbers by the DG, SD, and Huynh schemes via FR. However, for high wavenumbers, the Huynh, SD, and DG schemes via FR, in this order, struggle to approximate the exact relation. These results are consistent with those of Jameson [8].

4 Validation

4.1 2D Transports of chemical species

In this test case, we consider the transport of two chemical species, O_2 and N_2, with mass fractions $Y_{O_2}^0 = 0.23$ and $Y_{N_2}^0 = 0.77$ respectively, at the same temperature

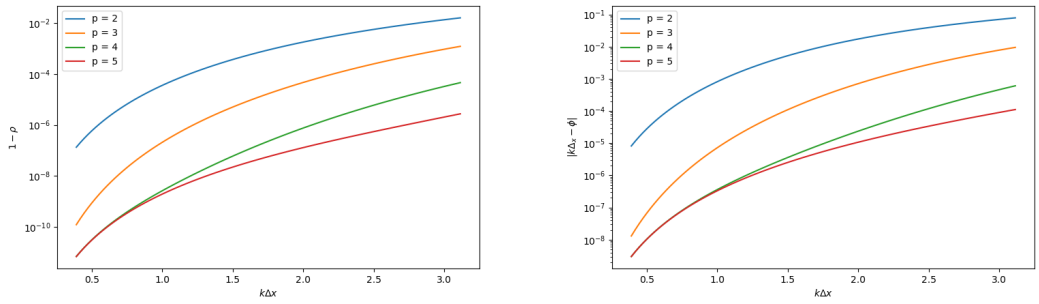

(a) (b)

Figure 4: Relations of (a) dissipation and (b) dispersion of the SD scheme via FR for $p \in \{2, 5\}$.

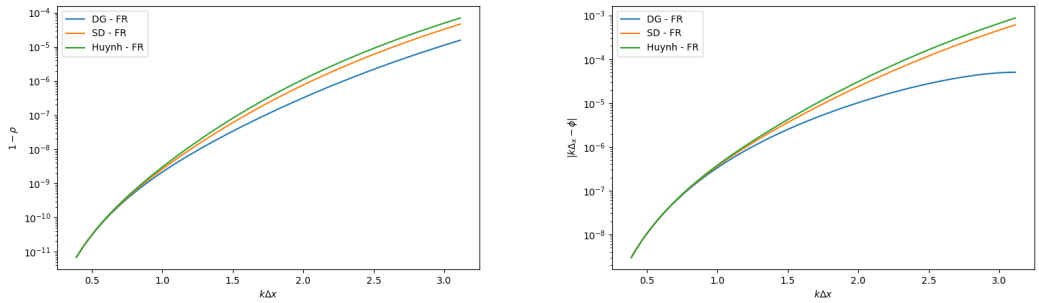

(a) (b)

Figure 5: Relations of (a) dissipation and (b) dispersion for the DG, SD, and Huynh schemes via FR for $p = 4$.

(T=300K), without accounting for any chemical reactions nor viscous forces. To avoid any numerical instability, the steps at the interface between both regions are smoothed out using hyperbolic exponential functions as follows

$$\phi(x, y, t) = \frac{\beta}{\sqrt{\dfrac{4\nu t}{\alpha^2} + 1}} \exp\left(-\frac{x^2}{4\nu t + \alpha^2}\right) \tag{28}$$

$$Y_{N_2} = Y^0_{N_2} - \phi, Y_{O_2} = Y^0_{O_2} + \phi. \tag{29}$$

The geometry is defined by a rectangle with a length $L = 0.02$ m and a width $l = 0.0004$ m. The adjustment parameters are taken as $\nu = 1 \times 10^{-3}$, $\beta = 0.1$, and $\alpha = 2 \times 10^{-3}$. The pressure is constant throughout the domain and equal to $P = 101325$ Pa, and the velocity field $\mathbf{V} = (100, 0)$ leads to convection of species at a constant velocity in the x-direction. Finally, periodic boundary conditions are imposed on each side of the geometry. Figure 6

displays the profiles of the mass fractions Y_{N_2} and Y_{O_2} after 10 convection times using the DG, SD, and Huynh schemes via FR with third-order accuracy in space (polynomial degree $p = 2$) and time (RK33). It is observed that the DG, SD, and Huynh schemes via FR, in that order, better approximate the exact mass fraction profiles, indicating that the numerical dissipation and dispersion properties are reduced with DG, SD, and Huynh schemes via FR, in that order. The spurious oscillations observed in the regions $-1 < x < -0.4$ and $0.5 < x < 1$ are related to the coarse nature of the mesh. These oscillations are more pronounced with the Huynh, SD, and DG schemes via FR, in that order. This suggests that for Large Eddy Simulation-type calculations, better results might be achieved with the DG scheme via FR, compared to SD and Huynh via FR. The results obtained are in good agreement with the numerical analysis presented in subsection 4.1.

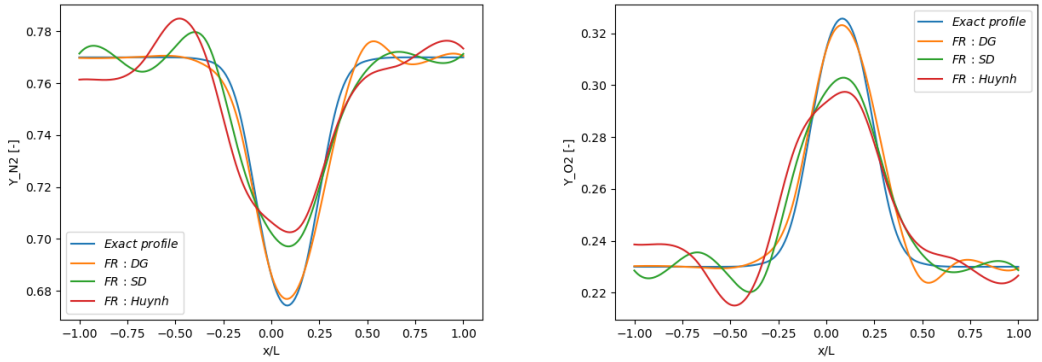

(a) (b)

Figure 6: Profiles of the mass fractions Y_{N_2} (a) and Y_{O_2} (b) after 10 periods with the DG, SD, and Huynh schemes via FR for $p = 2$.

4.2 3D Taylor Green Vortex

The Taylor-Green vortex (TGV) problem is a canonical problem for which a turbulent energy cascade can be observed numerically. We assume that $\Omega =]-\pi L_0, \pi L_0[^D$, with L_0 being the characteristic length. The physical quantities are made dimensionless using the reference quantities L_0, V_0, ρ_0 et T_0. The viscosity is derived from the Reynolds number

$$\mu = \frac{\rho_0 V_0 L_0}{\mathsf{Re}}. \tag{30}$$

We assume that at the initial time, the density is uniform in Ω and equal to ρ_0. The

initial velocity field is

$$V_1 = \quad V_0 \sin\left(\frac{x}{L_0}\right)\cos\left(\frac{y}{L_0}\right)\cos\left(\frac{z}{L_0}\right), \tag{31a}$$

$$V_2 = -V_0 \cos\left(\frac{x}{L_0}\right)\cos\left(\frac{y}{L_0}\right)\cos\left(\frac{z}{L_0}\right), \tag{31b}$$

$$V_3 = \quad 0. \tag{31c}$$

The initial pressure is

$$P = P_0 + \frac{\rho_0 V_0^2}{16}\left[\cos\left(\frac{2x}{L_0}\right) + \cos\left(\frac{2y}{L_0}\right)\right]\left[\cos\left(\frac{2z}{L_0}\right) + 2\right]. \tag{32}$$

For this test case, the following values were chosen

$$L_0 = \frac{1}{\pi}, \quad V_0 = \frac{1}{\pi}, \quad \rho_0 = 1, \quad \mathsf{Ma} = 0.1, \quad \mathsf{Pr} = 0.71 \quad \text{and} \quad \mathsf{Re} = 1600. \tag{33}$$

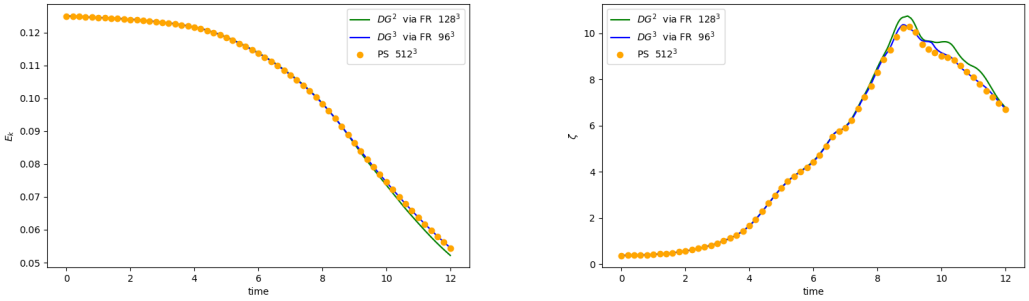

(a) (b)

Figure 7: Kinetic energy (a) and enstrophy (b) of the TGV at Re=1600: case of h,p-refinement with 384^3 degrees of freedom.

We propose in this case to compare polynomial order increase of FR schemes for a number of degrees of freedom equal to 384^3. The calculations performed in this case are on a 128^3 mesh with third-order accuracy in space ($p = 2$) denoted 128p2 and on a 96^3 mesh with four-order accuracy in space ($p = 3$) denoted 96p3. For both 128p2 and 96p3 calculations, we use the RK45 time discretization scheme. We compared the results of DG simulations via FR with those obtained from the Pseudo-Spectral PS code [15] on a 512^3 mesh. The simulations were carried out up to a time $t = 12$ s. Figure 7 shows the evolution of kinetic energy and enstrophy. It can be observed that DG calculations via FR reproduce the evolution of kinetic energy. The evolution of enstrophy is well represented by all calculations up to $t = 8.5$ s. After this time, the 128p2 calculation overestimates the evolution of enstrophy. The 96p3 calculation accurately reproduces the evolution of

enstrophy throughout the entire simulation time. However, it is noted that enstrophy curves are well reproduced by all calculations up to $t = 8.5$ s. After this time, the 128p2 calculation overestimates the evolution of enstrophy. The 96p3 calculation reproduces the evolution of enstrophy perfectly throughout the entire simulation time. This study demonstrates that it is possible to achieve a level of accuracy given by reference data on coarse meshes when using high order for a fixed number of degrees of freedom.

5 CONCLUSIONS

In this paper, we presented a spatio-temporal analysis of FR schemes, highlighting two main results. The first result focuses on the spatio-temporal analysis of the spectral properties of FR schemes, which is consistent with and complementary to the semi-discrete analysis conducted by Asthana et al [8]. We showed that dissipation and dispersion properties can be reduced through careful choices of the correction function parameters and by increasing the polynomial order. Finally, we extended and validated these results for academic configurations of multi-species flows and turbulent flows. The results presented in this article stem from the development of FR schemes that we implemented in the CONVERGE CFD [16] software.

The authors of this paper are aware that, to date, methodologies for extending FR schemes to multi-species flows, both reactive and non-reactive, as well as for h-p refinement adaptation, are still scarce in the literature. We have defined approaches for these topics that go beyond the scope of this paper and will be presented in our future work.

REFERENCES

[1] Z. Wang, K. Fidkowski, R. Abgrall, F. Bassi, D. Caraeni, A. Cary, H. Deconinck, R. Hartmann, K. Hillewaert, H. Huynh, N. Kroll, G. May, P.-O. Persson, B. van Leer, and M. Visbal, High-order CFD methods : Current status and perspective, Int. J. Numer. Meth. Fluids, 72 (2013), pp. 811–845, https://doi.or g/10.1007/s10915-010-9420-z .

[2] W. H. Reed and T. R. Hill, Triangular mesh methods for the neutron transport equation, Tech. Report LA-UR–73-479, Los Alamos National Laboratory, New Mexico, USA, October 1973, https://digital.library.unt.edu/ark:/67531/metadc1036080/.

[3] B. Cockburn, G. E. Karniadakis, and C.-W. Shu, The development of discontinuous Galerkin methods, in Discontinuous Galerkin Methods : Theory, Computation, and Application, B. Cockburn, G. E. Karniadakis, and C. W. Shu, eds., vol. 11 of Lecture Notes in Computational Science and Engineering, Springer, Berlin, 2000, pp. 3–50, https://doi.org/10.1007/978-3-642-59721-3 .

[4] J. S. Hesthaven and T. Warburton, Nodal Discontinuous Galerkin Methods : Algorithms, Analysis and Applications, vol. 54 of Texts in Applied Mathematics, Springer, New York, 2008, https://doi.org/10.1007/978-0-387-72067-8 .

[5] D. A. Kopriva and J. H. Kolias, A conservative staggered-grid Chebyshev multidomain method for compressible flows, J. Comput. Phys., 125 (1996), pp. 244–261, https://doi.org/10.1006/jcph.1996.0091.

[6] D. A. Kopriva, A conservative staggered-grid Chebyshev multidomain method for compressible flows. II. A semi-structured method, J. Comput. Phys., 128 (1996), pp. 475–488, https://doi.org/10.1006/jcph.1996.0225 .

[7] Y. Liu, M. Vinokur, and Z. J. Wang, Spectral difference method for unstructured grids I : Basic formulation, J. Comput. Phys., 216 (2006), pp. 780–801, https://doi.org/10.1016/j .jcp.2006.01.024.

[8] K. Asthana and A. Jameson,High-order flux reconstruction schemes with minimal dispersion and dissipation, J. Sci. Comput., 62 (2015), pp. 913–944, https://doi.org/10.1007/s10915-014-9882-5 .

[9] H. T. Huynh, A flux reconstruction approach to high-order schemes including discontinuous Galerkin methods, in 18th AIAA Computational Fluid Dynamics Conference, Miami, Florida, June 2007, https://doi.org/10.2514/6.2007-4079 .

[10] Castonguay, P. and Williams, D. M. and Vincent, P. E. and Jameson, A., Energy stable flux reconstruction schemes for advection–diffusion problems, Comput. Meth. Appl. Mech. Eng., 267,(2013), https://doi.org/10.1016/j .cma.2013.08.012 .

[11] Roe, Philip L., Approximate Riemann Solvers, Parameter Vectors, and Difference Schemes, J. Comput. Phys., 43, (1981), https://doi.org/10.1016/0021-9991(81)90128-5 .

[12] Lax, Peter D., Weak solutions of nonlinear hyperbolic equations and their numerical computation, Commun. Pure Appl. Math., 7, (1954), https://doi.org/10.1002/cpa.3160070112 .

[13] Friedrichs, Kurt Otto, Symmetric hyperbolic linear differential equations, Commun. Pure Appl. Math.,7,(1954), https://doi.org/10.1002/cpa.3160070206 .

[14] J. Vanharen, G. Puigt, X. Vasseur, J.-F. Boussuge, and P. Sagaut, Revisiting the spectral analysis for high-order spectral discontinuous methods, J. Comput. Phys., 337 (2017), pp. 379–402, https://doi.org/10.1016/j .jcp.2017.02.043.

[15] Cant, R., FERGUS, A user guide, Cambridge University Engineering Department, 1999.

[16] Richards, K.J., Senecal, P.K., and Pomraning, E., CONVERGE 3.1, Convergent Science, Madison, WI (2024).